Crosslinked ionogels containing a Li-conducting inorganic phase as electrolyte for lithium-metal batteries

Matteo Gandolfo [a], Mattia Longo [a], Thomas Diemant [b,c], Silvia Bodoardo [a], Dominic Bresser [b,c,d], Julia Amici [a,*]

[a] Department of Applied Science and Technology (DISAT), Politecnico di Torino, 10129 Torino, Italy
[b] Helmholtz Institute Ulm (HIU) Electrochemical Energy Storage, 89081 Ulm, Germany
[c] Karlsruhe Institute of Technology (KIT), 76021 Karlsruhe, Germany
[d] Ulm University (UUlm), 89069 Ulm, Germany

ABSTRACT

In the quest for the development of safer lithium-metal batteries (LMBs), the integration of inorganic fillers and ionic liquids into polymer matrices has emerged as a promising strategy to enhance safety, ionic conductivity and battery performance. This study introduces a novel composite ionogel (IG) synthesized through a facile one-pot method, incorporating butyl methacrylate (BMA) and poly(ethylene glycol) diacrylate (PEGDA) with the ionic liquid 1-butyl-1-methylpyrrolidinium bis(fluorosulfonyl)imide ($PYR_{14}FSI$) and garnet $Li_{6.4}La_3Zr_{1.4}Ta_{0.6}O_{12}$ (LLZTO) nanoparticles. A distinctive feature of the approach is the use of an organosilane functionalization of the LLZTO nanoparticles, which ensures their full integration into the polymer matrix during free-radical polymerization. Moreover, this method effectively eliminates the Li_2CO_3 passivation layer that typically forms on the surface of the LLZTO nanoparticles, thus, further contributing to an enhanced performance. As a result, a LMB with the functionalized LLZTO IG electrolyte delivered more than 160 mA h g^{-1} with a very good capacity retention of 97.7% after 400 cycles in Li|IG|LFP cells.

1. Introduction

Since the first studies on lithium-ion batteries (LIBs), dramatic improvements have been achieved for this technology with a huge impact on our daily lives. LIBs have driven the revolution of portable electronics, electric mobility and stationary energy storage, playing an important role in the energy transition towards a more sustainable future [1]. Despite being a rather recent invention, LIBs are about to reach the theoretical limits of intercalation electrode materials, while still struggling to meet the steadily increasing market needs, especially in the e-mobility sector [2,3]. Looking among the next-generation anodes, lithium metal is the most promising candidate and is considered the 'holy grail'. As a result of its very high theoretical specific capacity (3860 mA h g^{-1}), which is ten times higher than that of the presently used graphite (372 mA h g^{-1}), and a very low redox potential (−3.04 V vs. SHE), lithium-metal batteries (LMBs) may provide substantially higher

specific energy compared to LIBs [4–6]. Attempts to commercialize LMBs have been pursued in the 80 s; however, these cells were called back unveiling important safety issues [7,8]. It turned out that the utilized liquid electrolytes were unsuitable for LMBs because of the severe reactivity with lithium metal, the high flammability, and the sensitivity to dendritic lithium growth, causing the cell to short-circuit upon cycling with severe outcomes [9,10]. Lithium metal research was revitalized by the development of solid-state electrolytes (SSEs), which are anticipated to lead to an increased safety of these cells [11,12].

Polymer electrolytes are one of the most widely studied and promising candidates for room-temperature SSEs, with the first studies reported by Fenton et al. [13] and Armand et al. [14], dating back almost 50 years ago. To obtain good ionic conductivity also at room temperature, though, polymer matrices are frequently soaked with liquid phases, potentially affecting the safety of the cell. Additionally, most of the polymer electrolytes, including the intensively studied poly(ethylene oxide) (PEO), show limited stability towards oxidation, restricting their potential applications to low-voltage cathode materials such as LiFePO$_4$ (LFP) [15,16]. A potential solution is given by introducing ionic liquids (ILs)

* Corresponding author.
  E-mail address: julia.amici@polito.it (J. Amici).

into the polymer matrix, referred to as ionogel (IG). ILs, room-temperature organic molten salts, have peculiar physical and chemical properties such as low vapour pressure, reduced flammability, high thermal stability, and frequently a wide electrochemical stability window (ESW) [17–19]. IGs can inherit most of the properties of ILs while combining them with the typical advantages of polymers (e.g., flexibility, low cost, facile handling and processing) to form a promising candidate for safer next-generation LMBs. Despite the increased safety of IGs compared to liquid electrolytes, the physical entrapment of ILs, characterized by high viscosity and low transference number, affects the transport properties of the electrolyte, in particular, at elevated C rates. Typically, the Li salt dissociation in IL can be problematic and the formation of negatively charged ionic clusters can effectively drift the Li^+ in the wrong direction [20]. The addition of inorganic phases like SiO_2 [21], TiO_2 [22], Al_2O_3 [23], and ZrO_2 [24], which have essentially only a plasticizing effect on the polymer matrix, can also positively influence lithium salt dissociation, thus boosting the performance [25]. In a previous work [26], we developed a crosslinked IG investigating the introduction of Al_2O_3 nanoparticles. The inorganic filler reduced the polarization of the Li|IG|LFP cell promoting the formation of a stable interface and interphase on the electrodes and favouring the lithium salt dissociation. Due to the plasticizing effect of the IL ($PYR_{14}TFSI$) and Al_2O_3, the IG showed an ionic conductivity of $2.05 \cdot 10^{-4}$ S cm^{-1} at 20 °C, while displaying electrochemical stability towards oxidation up to 5.1 V vs. Li^+/Li. As a result, the Li|IG|LFP cells provided a specific capacity of 125 mA h g^{-1} at room temperature with a decent capacity retention of 94% after 100 cycles.

Since the development of sodium super ion conductors (NASICON) by Goodenough et al. [27], huge efforts have been devoted to study ceramic oxide electrolytes with different crystal structures, incl. perovskite-type, lithium super ion conductor (LISICON-type), lithium phosphorus oxynitride (LIPON-type) and garnet-type [28,29]. These ceramic electrolytes possess promising ionic conductivities (10^{-3}–10^{-4} S cm^{-1} at 25°C), relatively wide electrochemical stability windows and a transference number of unity ($\sim$1). However, their brittleness, reactivity with lithium metal and high interfacial impedance are still challenges that need to be overcome [30,31]. While the direct use of ceramic oxides as SSEs is challenging, their application as active filler in polymer electrolytes has gained extensive interest [32–34]. The transport pathways of Li^+ through these hybrid electrolytes are multiple and appear to be dependent, amongst others, on the filler concentration and the presence of a plasticizer [35]. By combining an active filler and IG, a new class of composite polymer electrolytes (CPEs) with intriguing electrochemical performance can be obtained. These active fillers can promote Li^+ transport kinetics while the IL can increase the overall safety of the cell. Zhai et al. [36] studied for the first time a hybrid silica-LLZO IG using PEO as the polymer host matrix, reporting a high ionic conductivity of 7.4×10^{-4} S cm^{-1} at 25 °C and an extended electrochemical stability towards oxidation of up to 5.5 V vs. Li^+/Li. The IG could also actively suppress the dendrite formation at elevated temperature (55 °C) and showed a rather high limiting current density of 0.7 mA cm^{-2}. The eventually studied 4 V Li||LFP quasi-solid battery cell delivered a specific discharge capacity of 135 mA h g^{-1} after 100 cycles. In another work, Guo et al. [37] developed an active composite IG comprised of 50 wt% NASICON-type Li$_{1+x}$Al$_x$Ge$_{2-x}$(PO$_4$)$_3$ (LAGP) nanoparticles, 1-ethyl-3-methylimidazolium bis(trifluoromethylsulfonyl)imide (EMIM TFSI) and lithium bis(trifluoromethylsulfonyl)imide (Li TFSI) using poly(vinylidene fluoride-co-hexafluoropropylene) (PVdF-HFP) as the host matrix. The ionic conductivity was close to 1 mS cm^{-1} and the IG was stable up to 4.8 V vs. Li^+/Li, providing 152 mA h g^{-1} at 0.05C in Li||LFP cells. However, the impedance increased upon cycling, underlining a possible reactivity between the lithium metal and the electrolyte.

Herein, we present composite IGs prepared via a one-pot preparation method by mixing the polymer precursors BMA and PEGDA with the IL $PYR_{14}FSI$ and garnet LLZTO nanoparticles. The inorganic filler has been fully integrated into the polymer matrix by using an organosilane surface functionalization. The results underline the importance of functionalizing such inorganic phases when introducing them into polymers to improve the Li^+ transport kinetics, while removing the Li_2CO_3 passivating layer on LLZTO nanoparticles.

2. Experimental section

2.1. Synthesis of ionogels

All ionogels (IGs) were prepared by a one-pot free radical polymerization in an argon-filled glovebox (O_2 and H_2O level < 0.5 ppm). All the precursors were degassed under vacuum and stored in an argon-filled glovebox. Molecular sieves were added to trap the residual water present in the precursors. The polymer backbone composed of butyl methacrylate (BMA) (Acros Organics) and poly(ethylene glycol) diacrylate (PEGDA) (average M_n = 575, Sigma-Aldrich) in a weight ratio 8:2 was formed by adding 0.05 wt% benzoyl peroxide (BPO) (75%, Acros Organics) in presence of 1-butyl-1-methylpyrrolidinium bis(fluorosulfonyl)imide (PYR_{14}-FSI) (Solvionic) and lithium bis(trifluoromethanesulfonyl)imide (LiTFSI) (Solvionic). The weight ratio between the polymer matrix, $PYR_{14}FSI$ and LiTFSI was set to 1:2:0.6. Different amounts of silane-modified Li$_{6.4}$La$_3$Zr$_{1.4}$Ta$_{0.6}$O$_{12}$ (LLZTO, MTI D50 $\approx$ 400 nm) nanoparticles were added and the developed formulations were labelled as *x*% LLZTO, where *x*% is the weight percentage of LLZTO compared to the polymer matrix. After adding all the components in a vial, the formulation was mixed under moderate stirring for 1 h at room temperature. The temperature was then increased to 60 °C, keeping a moderate stirring for 30 min. The mixture was cast into a lidded Petri dish and kept at 60 °C for 20 h. The obtained IGs were cut (thickness of 250–300 μm) and used for further characterization.

2.2. Fabrication of silane-modified LLZTO

Silane-modified LLZTO was prepared following the protocol proposed by Yan et al. [38]. The silane precursor solution consisted of 2.5 vol% 3-(trimethoxysilyl) propyl methacrylate (TPM), 2.5 vol% acetic acid, 5 vol% water and 90 vol% ethanol, and was stirred for 1 h to form the reactive silanol ends. Pristine LLZTO nanoparticles (600 mg) were then added to the silane precursor solution (40 mL) and kept stirring for 6, 15, and 24 h at 70 °C. Modified LLZTO nanoparticles, named LLZTO 6 h, LLZTO 15 h and LLZTO 24 h, were then collected by centrifugation at 6000 r min^{-1} for 10 min and washed three times with ethanol.

2.3. Preparation of the LFP cathodes

The LFP cathodes were prepared by mixing LFP (Aleees), carbon black (C-NERGY C65, Imerys) and polyvinylidene difluoride (PVdF, HSV900, Arkema) in a 7:2:1 wt ratio with *N*-methyl pyrrolidone (NMP) as solvent. A mixer mill (Retsch® MM40) and zirconia spheres were used to homogenize the slurry, which was deposited on a carbon-coated Al foil with a 200 μm doctor blade film applicator and dried at 50 °C for 60 min. The LFP electrodes were obtained with a 15 mm cutter, dried under vacuum at 120 °C for 8 h and stored in an argon-filled glovebox. The mass loading was set to about 2.0 mg cm^{-2}.

2.4. Physicochemical characterisation

The morphology of the pristine and functionalized LLZTO was studied by scanning electron microscopy (SEM) using a Zeiss SUPRA TM 40 with a Gemini column and a Schottky field emission tip (tungsten at 1800 K). Energy-dispersive X-ray spectroscopy (EDS) was performed for the elemental composition analysis. All samples were sputtered with a 4 nm layer of platinum before the SEM measurements. The thickness of the organosilane layer was measured with a scanning transmission electron microscope ((S)TEM, Thermo Scientific Talos F200X) equipped with a field emission gun XFEG. Thermogravimetric analysis (TGA, Model Q5000, TA Instruments) was performed to quantify the amount of organosilane functionalizer added to the LLZTO and the thermal stability of the IGs. The samples were heated from 40 °C to 800 °C at a heating rate of 10 °C min^{-1} under 25 mL min^{-1} N$_2$ flow for the IGs and under 25 mL min^{-1} N$_2$:O$_2$ 8:2 for LLZTO. Attenuated total reflection Fourier transform infrared spectroscopy (ATR-FTIR, Nicolet™ iS50 FTIR spectrometer, Thermo Scientific) was used to identify the absorption peaks of the organosilane functionalizer grafted to the LLZTO. The spectra were collected in the range from 425 to 4000 cm^{-1} with 32 scans and at 4 cm^{-1} resolution. In addition, the organosilane functionalization was also identified by an inVia™ confocal Raman microscope (Renishaw) equipped with a 50 mW green laser (532 nm). Two different spectra were obtained in the 10–4000 and 1000–2000 cm^{-1} Raman shift range with 5% laser power. The investigation of the crystal structure for the pristine and functionalized LLZTO was conducted via X-ray diffraction (XRD) using a Bruker D8 Advance diffractometer (Cu-K$_\alpha$ radiation, λ = 0.154 nm) equipped with a graphite monochromator within a 2θ range from 10° to 90°. X-ray photoelectron spectroscopy (XPS) measurements were performed in a Specs ultrahigh vacuum surface analysis system (10^{-10} mbar) with a Phoibos 150 XPS spectrometer. The spectra were recorded using monochromatic Al-K$_\alpha$ radiation (300 W) and pass energies of 90 and 30 eV for survey and detail scans, respectively. Neutralization was required; the main C 1s peak was set to 284.8 eV for binding energy calibration. The peak fitting was carried out using the CasaXPS software with Shirley-type backgrounds and a peak shape based on a Gaussian-Lorentzian product function (GL30). Inductively coupled plasma optical emission spectroscopy (ICP-OES) was conducted on a Spectro Arcos spectrometer (Spectro Analytical Instruments) to investigate the lithium leaching. For these measurements, bare LLZTO and silane-functionalized powders were treated in aqua regia and digested in a microwave. The solution was then filtered and analysed via ICP-OES.

2.5. Electrochemical characterization

Electrochemical impedance spectroscopy (EIS) measurements were carried out in the 100 kHz–Hz frequency range at open-circuit voltage (OCV) with a 10 mV amplitude using a VSP-3e potentiostat (Biologic). For the determination of the ionic conductivity, symmetric cells were assembled with two stainless steel blocking electrodes (SS|IG|SS) in ECC-Std test cells (EL-CELL GmbH). Measurements were performed at different temperatures in the range of 20–60 °C with a 10 °C sampling interval in a climatic chamber (MKF 56, Binder). The ionic conductivity (σ) was determined according to Eq. (1).

$$\sigma = \left(\frac{l}{A}\right) \cdot \left(\frac{1}{R_s}\right) \tag{1}$$

where l is the membrane thickness, A is the membrane surface area and R_s is the resistance value at the high-frequency intercept. Linear sweep voltammetry (LSV) was applied on Li|IG|SS ECC-Std test cells (EL-CELL GmbH) in the 2.0 to 6.0 V voltage range with a sweep rate of 0.1 mV s^{-1} using a VSP-3e potentiostat (Biologic). The electrochemical stability window (ESW) was determined by the intersection of the curve obtained with a 5 μA cm^{-2} horizontal line. Cyclic voltammetry (CV) was performed in Li|IG|LFP half-cells with ECC-Std test cells using a VSP-3e potentiostat (Biologic). The IG compatibility with the electrodes was evaluated in the 2.5–4.2 V potential range at a sweep rate of 0.1 mV s^{-1}. Lithium stripping and plating tests were conducted at 40 °C in CR2032coin cells assembled by sandwiching the IG electrolyte between two 12 mm lithium electrodes (Li|IG|Li). The current density was set to 0.05 mA cm^{-2} for 50 cycles, before increasing it to 0.1 mA cm^{-2}. EIS was used to reveal the evolution of interfaces before and after stripping and plating tests. The frequency range was set to 100 kHz–0.1 Hz and the tests were performed at OCV using a VSP-3e potentiostat (Biologic) with a 10 mV amplitude. EIS spectra were fitted using Zview software. Cycling tests were performed with an Arbin BT-2000 battery tester using ECC-Std test cells in half-cell configuration with LFP cathodes at 40 °C. After three formation cycles at 0.1 C, the C rate was increased to 0.2 C for the following cycles.

3. Results and discussions

3.1. Ionogel preparation

Cross-linked self-standing composite IGs were synthesised using a one-pot preparation method illustrated in Section 2.1 and
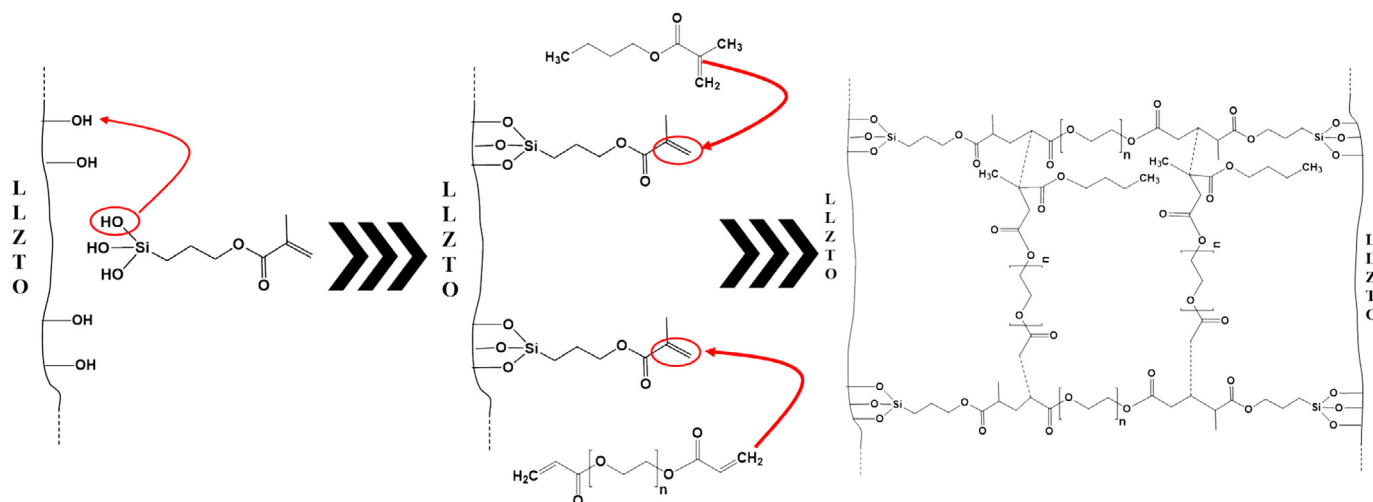

Fig. 1. Schematic of the synthesis procedure of functionalized LLZTO and their integration into the polymer matrix.

LLZTO was introduced by physical mixing with the polymer precursors. Garnets such as LLZTO are highly sensitive to moisture, forming a Li_2CO_3/LiOH resistive layer at the surface, which causes slow Li^+ kinetics and heterogenous lithium deposition [39]. The reaction involves H_2O and CO_2, with the two-step reaction forming initially LiOH in a Li^+/H^+ exchange reaction followed by a carbona-
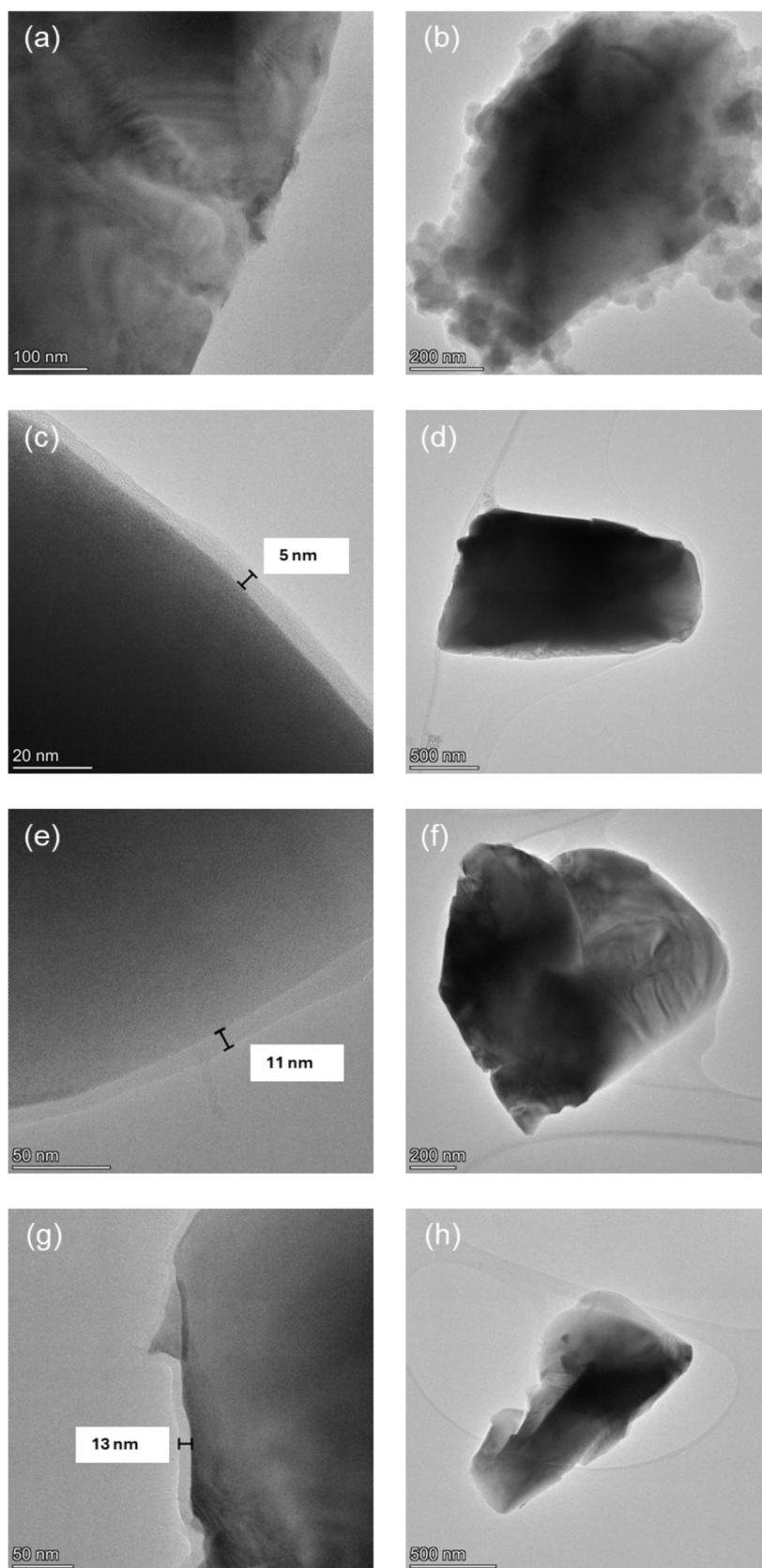
Fig. 2. TEM micrographs of (a, b) bare LLZTO, (c, d) LLZTO 6 h, (e, f) LLZTO 15 h, and (g, h) LLZTO 24 h.

tion reaction being a more favourable route compared to direct carbonation [40]. The Li_2CO_3/LiOH outer shell of LLZTO was converted into an acidic environment and a silane functionalizer, 3-(trimethoxysilyl)propyl methacrylate (TPM), was added. As illustrated in Fig. 1, the formed hydroxyl groups from Li_2CO_3 decomposition were grafted with TPM via a condensation reaction, and directly crosslinked within the polymer matrix during the IG synthesis.

3.2. Characterization of silane-modified LLZTO

Three different functionalized LLZTO NPs were produced by increasing the reaction time and the silane amount grafted. The obtained materials were named LLZTO 6 h, LLZTO 15 h, and LLZTO 24 h, according to the reaction time. After cleaning and drying, the garnet particles were studied via field emission SEM. As shown in Fig. S1a–f, the unmodified LLZTO particles are characterized by an irregular surface, presumably indicative of reaction products with moist air, while the functionalized LLZTO exhibit a smoother surface without extensive irregularities, indicating that the surface impurities got washed away in the acidic environment during functionalization. Energy dispersive X-ray spectroscopy (EDS)

(Fig. S2a–d) was applied for the elemental analysis, but the overlap between the Ta and Si peaks posed serious problems in TPM identification, while C and O peaks could not be used directly because they are also present in the LLZTO surface products. Nonetheless, some conclusions can still be drawn concerning the element abundance. La is the most abundant metal in LLZTO after Li and the theoretical O to La atomic ratio is 4:1. Assuming that the La concentration is constant, it is possible to track the relative abundance of O in every sample. A reduction of the relative O content could be ascribed to the conversion of LLZTO surface products during the functionalization. The O/La atomic ratio in pristine LLZTO was measured as 13.1, which is much higher than the theoretical one. When increasing the reaction time, it decreases to 9.1, 7.0, and 5.7 for LLZTO 6 h, LLZTO 15 h, and LLZTO 24 h, respectively. The O/La reduction could be ascribed to the conversion of the oxygen-rich surface species like Li_2CO_3 during the functionalization reaction. The organic coating thickness was measured by transmission electron microscopy (TEM). As shown in Fig. 2a–h, the thickness increased from about 5 nm for LLZTO 6 h to 11 and 13 nm for LLZTO 15 h and 24 h, respectively. The functionalization rate appears to be higher for the first reaction hours, while a slight difference is present for LLZTO 15 h and 24 h, indicating a certain
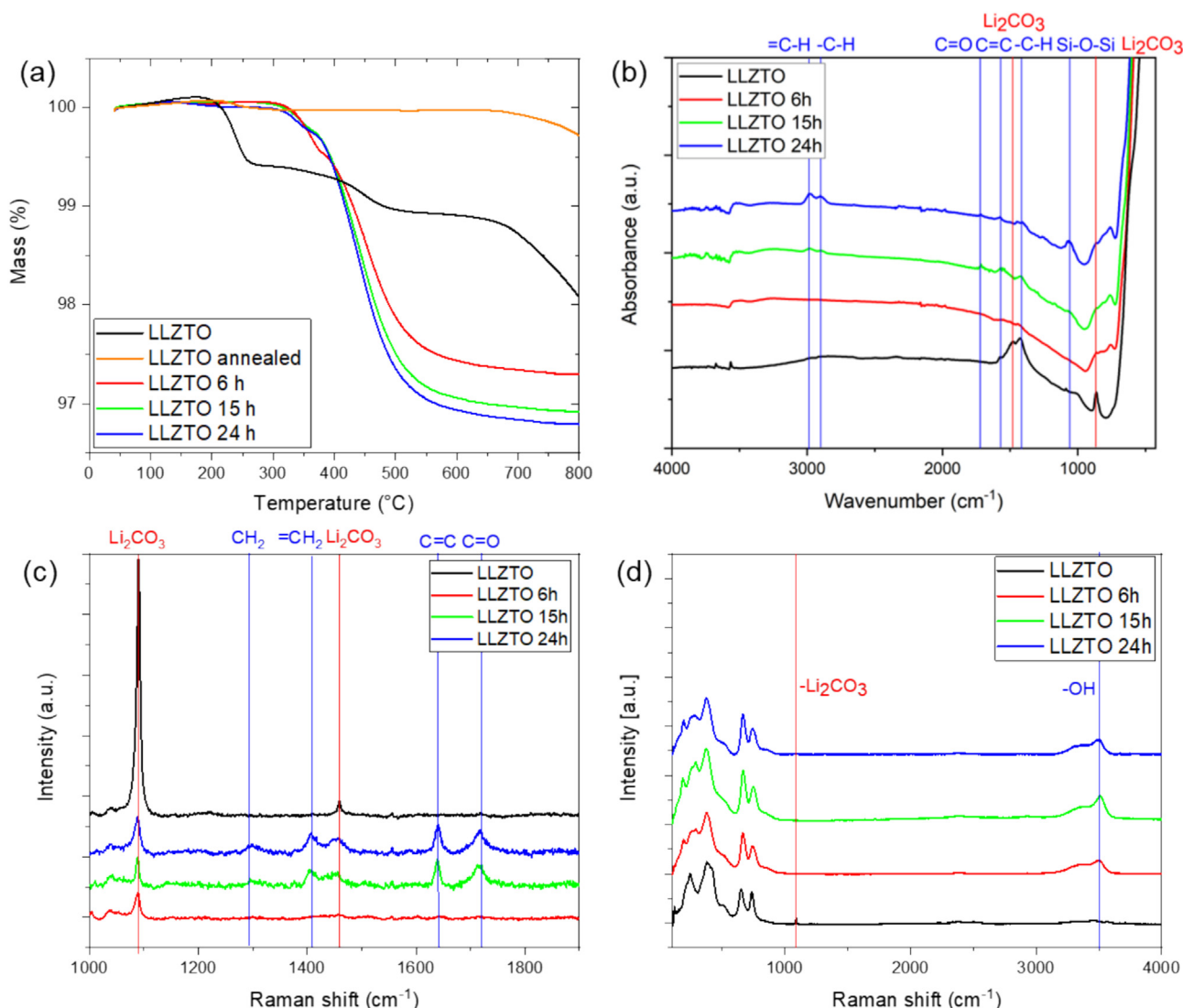

Fig. 3. (a) Thermograms, (b) FTIR and (c, d) Raman spectra of bare and functionalized LLZTO.

degree of saturation after 15 h. Looking at the surface of the bare LLZTO (Fig. 2a, b), many particles are covered by a thick and irregular reaction layer as already observed by SEM.

Weight quantification of organic moieties grafted on LLZTO NPs was performed by using thermo-gravimetric analysis (TGA) under constant airflow. As demonstrated in Fig. 3a, the bare LLZTO ther-

mogram presents a small weight increase and three main weight losses: the weight increase between 150–200 °C can be ascribed to the formation of LiOH on the surface of inorganic fillers due to the presence of residual water, the first weight loss at 190 °C can be ascribed to the elimination of chemisorbed water (~0.55%), the second loss at 410 °C is identified as the conversion of LiOH
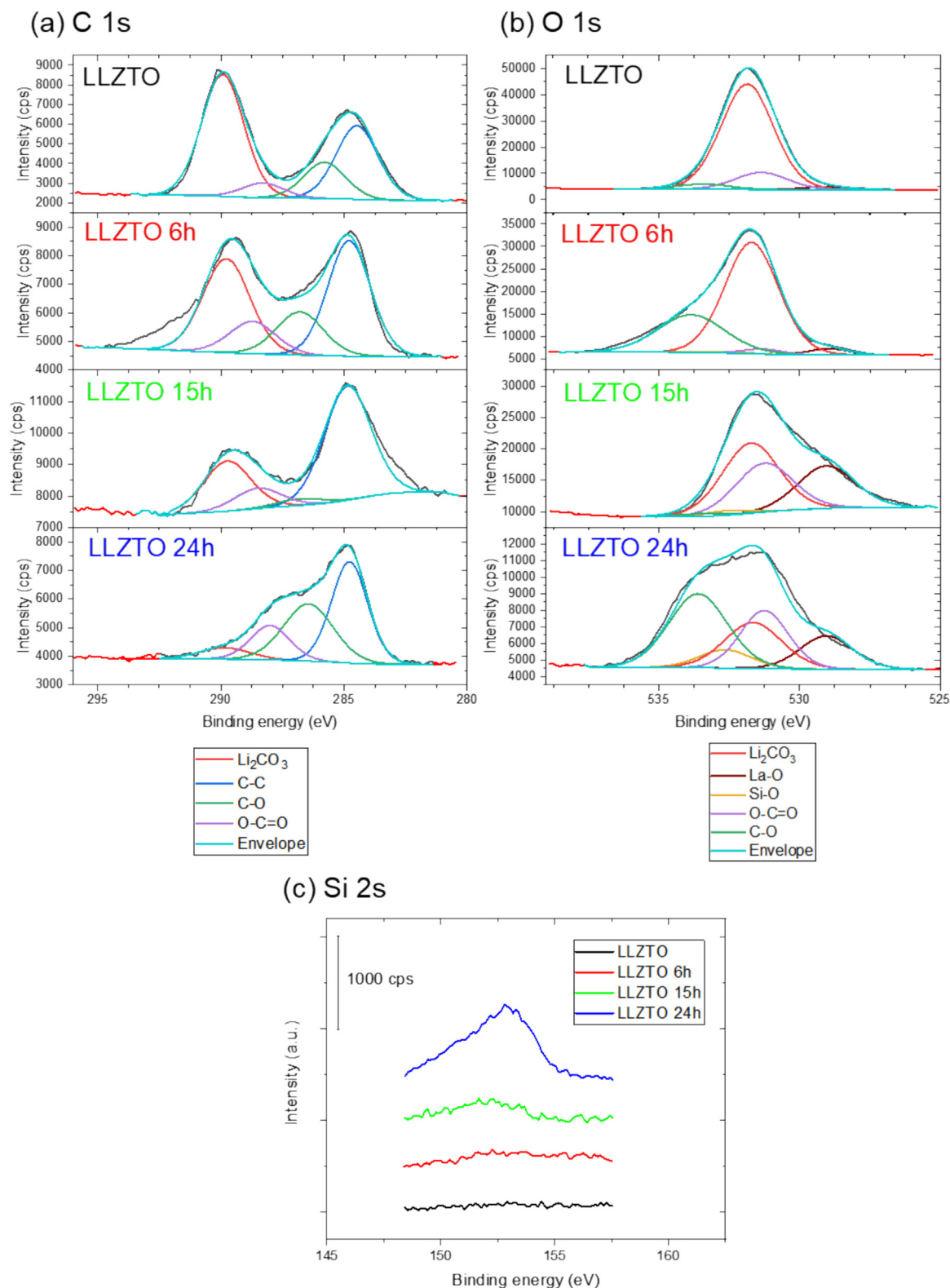

Fig. 4. XPS detail spectra in the (a) C 1s, (b) O 1s and (c) Si 2s regions of bare and functionalized LLZTO.

to Li_2O with water release ($\sim 0.3\%$), while the third loss is assigned to the degradation onset at 650 °C due to Li_2CO_3 decomposition with CO_2 formation [41]. As confirmation of these hypotheses, LLZTO was annealed at 800 °C to remove the $Li_2CO_3/LiOH$ surface layer completely. As shown in Fig. 3a, annealed LLZTO presents no weight increase and a limited weight loss, compared to bare LLZTO in the Li_2CO_3 decomposition region, probably formed during furnace cooling time. The weight of the organic moieties increased with the functionalization time, following a non-linear behaviour, i.e., up to 3.2% for LLZTO 24 h. LLZTO 15 h and 24 h present a 0.13% weight gap, while LLZTO 6 h has a 0.5% weight gap compared to LLZTO 24 h. As demonstrated via TEM, these results indicate that the functionalization reaction occurs preferentially in the first reaction hours with a saturation effect after 15 h. The absence of a significant weight drop in the Li_2CO_3 decomposition region for the functionalized LLZTO confirms the essentially complete conversion of the resistive layer during the functionalization.

The nature of the surface groups on pristine and functionalized LLZTO was assessed by ATR-FTIR. As shown in Fig. 3b, the spectrum recorded on unmodified LLZTO NPs present two distinctive Li_2CO_3 peaks at 860 and 1490 cm^{-1}. After acidic treatment, the spectra of functionalized LLZTO display the disappearance of the Li_2CO_3 peaks and the appearance of specific TPM absorption bands at 1060, 1414, 1570, 1715, 2900, and 3000 cm^{-1}, which can be assigned to Si–O stretching, C–H bending, C=C stretching, C=O stretching, C–H stretching, and =C–H stretching vibrations, respectively. Such absorption bands are increasingly detectable for LLZTO 15 h and 24 h, while LLZTO 6 h shows a peculiar feature in the fingerprint region in line with other functionalized samples. The garnet powders were also characterized by Raman spectroscopy applying a 532 nm green laser. The results are shown in Fig. 3c, d and are in line with the IR spectroscopy data: bare LLZTO shows distinctive Li_2CO_3 peaks at 1087 and 1460 cm^{-1} due to the symmetric and asymmetric stretching mode of CO_3^{2-}, respectively. The carbonate peak intensity decreases and characteristic peaks of the organic moieties appear for the functionalized LLZTO. The peaks at 1403, 1453, 1639, and 1715 cm^{-1} can be assigned to $=CH_2$ bending, CH_3 bending, C=C stretching, and C=O stretching, respectively. Although LLZTO 6 h shows compared to the other samples a rather low peak intensity, the survey Raman spectra in the 100–4000 cm^{-1} range exhibit a large –OH peak due to unreacted hydroxyl group, which is not detectable for bare LLZTO. These results suggest that the functionalization can effectively convert the resistive Li_2CO_3 layer into hydroxyl groups, offering an exploitable anchor point for organosilanes.

These findings were further confirmed by the XPS analysis presented in Fig. 4a–c. Bare LLZTO shows a large Li_2CO_3 peak located at 289.8 eV, suggesting the formation of a carbonate layer at the surface of the LLZTO nanoparticles after exposure to moist air. This layer is converted during the TPM functionalization, as we observe a reduction of the Li_2CO_3 peak intensity when increasing the reaction time. The C 1 s spectra show also C–C, C–O, and O–C=O peaks at 284.8, 286.4, and 288.2 eV, respectively. Li_2CO_3 can also be identified in the O 1 s spectrum at 531.7 eV, showing a decrease in peak intensity when increasing the functionalization time. Moreover, the functionalized LLZTO showed the opposite trend for the Si–O peak at 532.6 eV in the O 1 s spectra, confirming the grafting of TPM to LLZTO. The rest of the O 1 s peaks can be identified as La–O, O–C=O, and C–O at 529.0, 531.3, and 533.5 eV, respectively. Finally, the presence of silicon is also detected in the Si 2 s spectra of LLZTO 24 h and LLZTO 15 h (Fig. 4c, Si 2p region cannot be used due to overlap with the La 4d peak), confirming the surface modification.

Next, ICP-OES was applied to determine the content of Li in functionalized LLZTO. The measured lithium content in LLZTO was 5.5 wt%, while for functionalized NPs it decreased linearly to 3.4 wt%, 3.0 wt%, and 2.7 wt% for LLZTO 6 h, LLZTO 15 h, and LLZTO 24 h, respectively. Considering that the theoretical lithium content for $Li_{6.4}La_3Zr_{1.4}Ta_{0.6}O_{12}$ is 5 wt%, in the last case, lithium depletion may severely affect the ion conduction capabilities of functionalized garnet particles. We may note that these values have to be taken with a certain caution in terms of "absolute values", as the LLZTO samples were not fully dissolved prior to the measurements. However, as all samples behaved the same, we may assume that the overall trend is correct and reliable.

The structural integrity of LLZTO after functionalization was verified with X-ray diffraction (XRD). As illustrated in Fig. S3, bare LLZTO shows the characteristic garnet *Ia-3d* space group diffraction pattern. Additional reflections at 32° and 35° originate from Li_2CO_3 contaminations that are eliminated after the functionalization. The functionalized LLZTO presents the same diffraction patterns as bare LLZTO, indicating the retention of the same space group with no lattice distortion after the functionalization process. The nucleation of new crystalline phases after the LLZTO leaching may also be excluded as no other reflections are observed.

3.3. Characterization of active composite ionogels

Functionalized garnet active fillers were introduced into the IG membranes by physical mixing with polymer precursors. The IL-
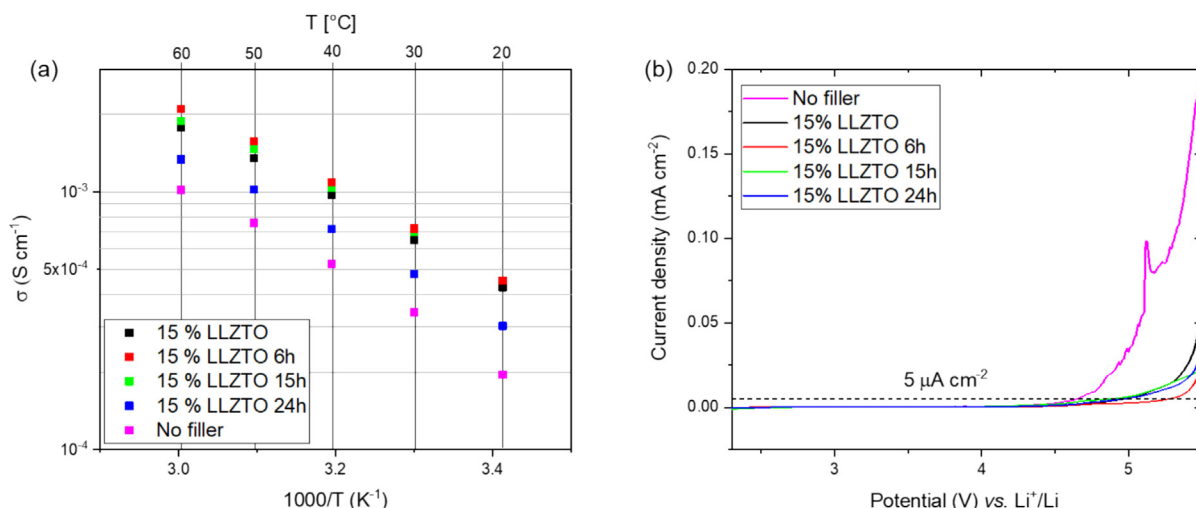

Fig. 5. (a) Ionic conductivity of different IGs. (b) Linear sweep voltammetry towards oxidation conducted on the different IGs investigated herein.

to-polymer weight ratio was set to 2:1 to obtain a sufficiently high ionic conductivity, while maintaining suitable mechanical properties in order to guarantee a good structural integrity. Higher IL ratios result in poor mechanical properties owing to the accordingly lower polymer content, rendering the handling challenging, while lower IL contents lead to electrolyte systems with a relatively low ionic conductivity and high interfacial resistance. The BMA to PEGDA molar ratio was set to 16:1 in order to produce a flexible matrix with large voids among the polymer chains able

to accommodate a high IL content. LLZTO was introduced by mixing it with the polymer precursors, obtaining composite IGs with a uniform filler distribution after synthesis. Several studies [42–45] were reported on hybrid electrolytes investigating the impact of the filler content on the ionic conductivity and cycling performance, identifying the optimum filler content between 10 wt% and 20 wt%. Hence, in our work, the inorganic filler concentration was set to 15 wt%. The filler dispersion within the polymer matrix was investigated via SEM. Fig. S4a–d show that the unmodified
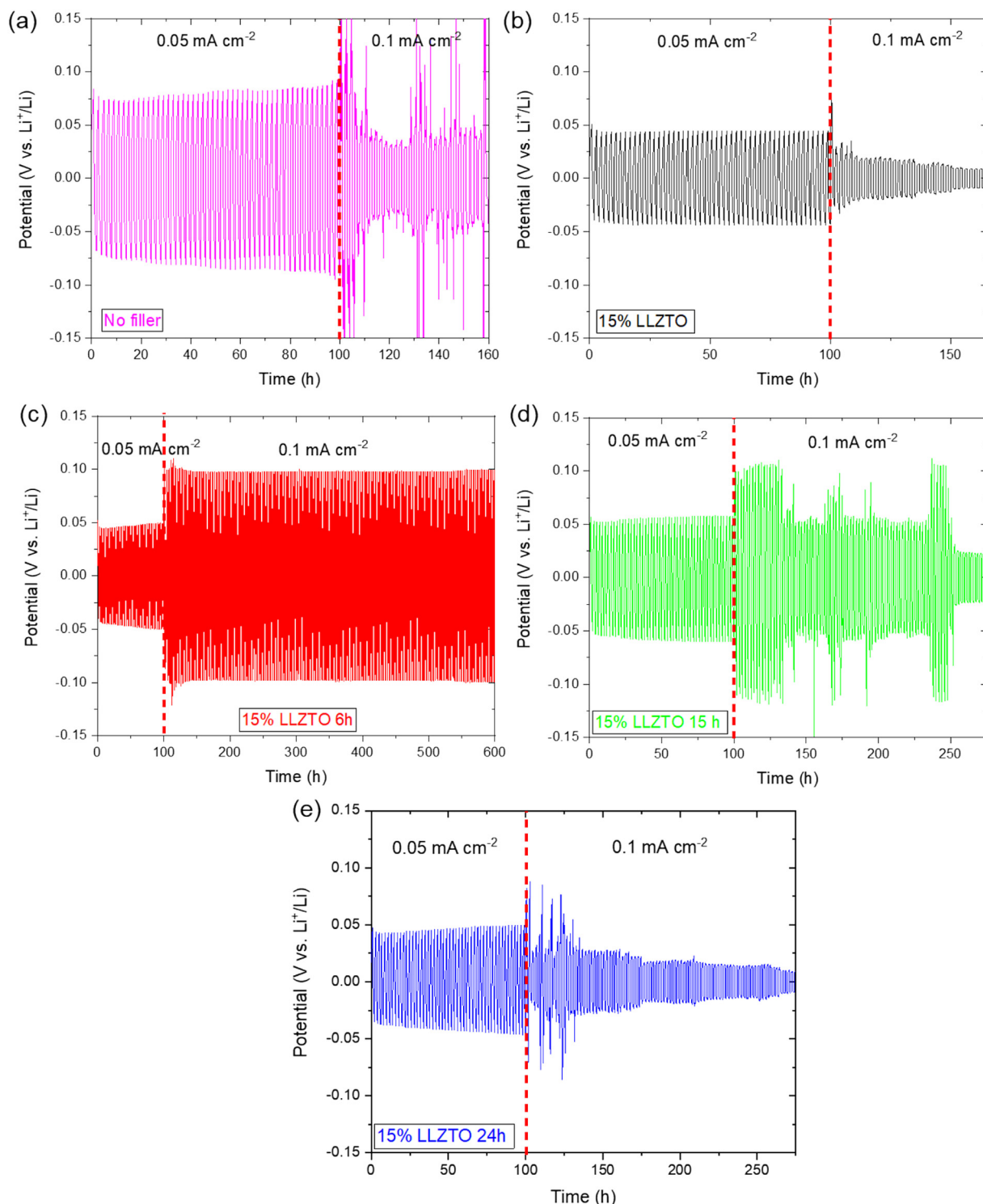

Fig. 6. Stripping/plating tests at 40 °C for (a) 'no filler', (b) 15% LLZTO, (c) 15% LLZTO 6 h, (d) 15% LLZTO 15 h, and (e) 15% LLZTO 24 h.

LLZTO forms agglomerates of about 5–6 μm in 15% LLZTO IGs. The inorganic particles appear to protrude out of the electrolyte membrane, displaying a scarce integration within the polymer matrix. The functionalized LLZTO nanoparticles present a better inclusion in the polymer. 15% LLZTO 6 h displays a reduced amount of filler agglomerates with a smaller size compared to 15% LLZTO 15 h and 24 h. In addition, the particles show an optimum integration into the polymer matrix, completely enveloping the inorganic filler. In this case, the functionalizer grafted to LLZTO plays an important role by forming a chemical bond with the polymer chains. The successful grafting of LLZTO particles to the polymer matrix was confirmed via ATR-FTIR, which showed no residual double bonds (C=C) (Fig. S5), therefore confirming the close to complete conversion of the double bond and the successful crosslinking. TG analysis (Fig. S6) was performed to check the inorganic filler content. The residual mass was around 7 % for IGs with functionalized and non-functionalized LLZTO, while 'no filler' IG presented a 2% residual mass. These results are coherent considering that the 15% LLZTO filler loading was calculated on the basis of the polymer part only, and that the overall IG is composed of roughly 72% IL fraction. The thermograms present four main weight drops: the first one at 220 °C for composite IGs and at 180 °C for 'no filler' IG can be assigned to the polymer chain decomposition, while the second one at 310 °C, the third one at 390 °C, and the fourth one at 590 °C may be ascribed to the decomposition of $PYR_{14}FSI$, LiTFSI and previously formed char, respectively. For all the degradation

pathways described, the inorganic filler plays a physical protection role by extending the degradation onset.

The composite IGs were subsequently tested electrochemically to investigate the role of LLZTO and the TPM functionalizer. The ionic conductivity plot (Fig. 5a) shows a Vogel-Tammann-Fulcher (VTF) behaviour. This non-Arrhenius-type behaviour is related to the ionic liquid portion of the IGs [46]. Generally, though, benefiting from the presence of the IL and its plasticizing effect, the IGs present a quite high ionic conductivity at 20 °C of $> 10^{-4}$ S cm^{-1}, and even 10^{-3} S cm^{-1} at 60 °C. The insertion of LLZTO increases the ionic conductivity by a factor of ~ 2 at 20 °C compared to 'no filler' IG, while the functionalization seems to be effective for 15% LLZTO 6 h, since the highest ionic conductivity is obtained in this case. The presence of the organosilane coating favours more efficient Li$^+$ pathways, limiting the particles agglomeration and decreasing the filler-polymer interfacial resistance by converting the Li$_2$CO$_3$-rich surface layer into a polymer compatible organic layer. In the case of 15% LLZTO 24 h, a reduction of the ionic conductivity compared to pristine LLZTO may be caused by the formation of a thick silane layer as well as the modification of garnet NPs due to lithium etching. The anodic stability against lithium metal is a fundamental prerequisite for electrolytes and the current research trend is to extend it over 5 V to increase cell energy density. The IGs are characterized by larger ESWs thanks to the presence of the IL and the insertion of the inorganic phase. The ESW was measured with linear sweep voltammetry, sandwiching the
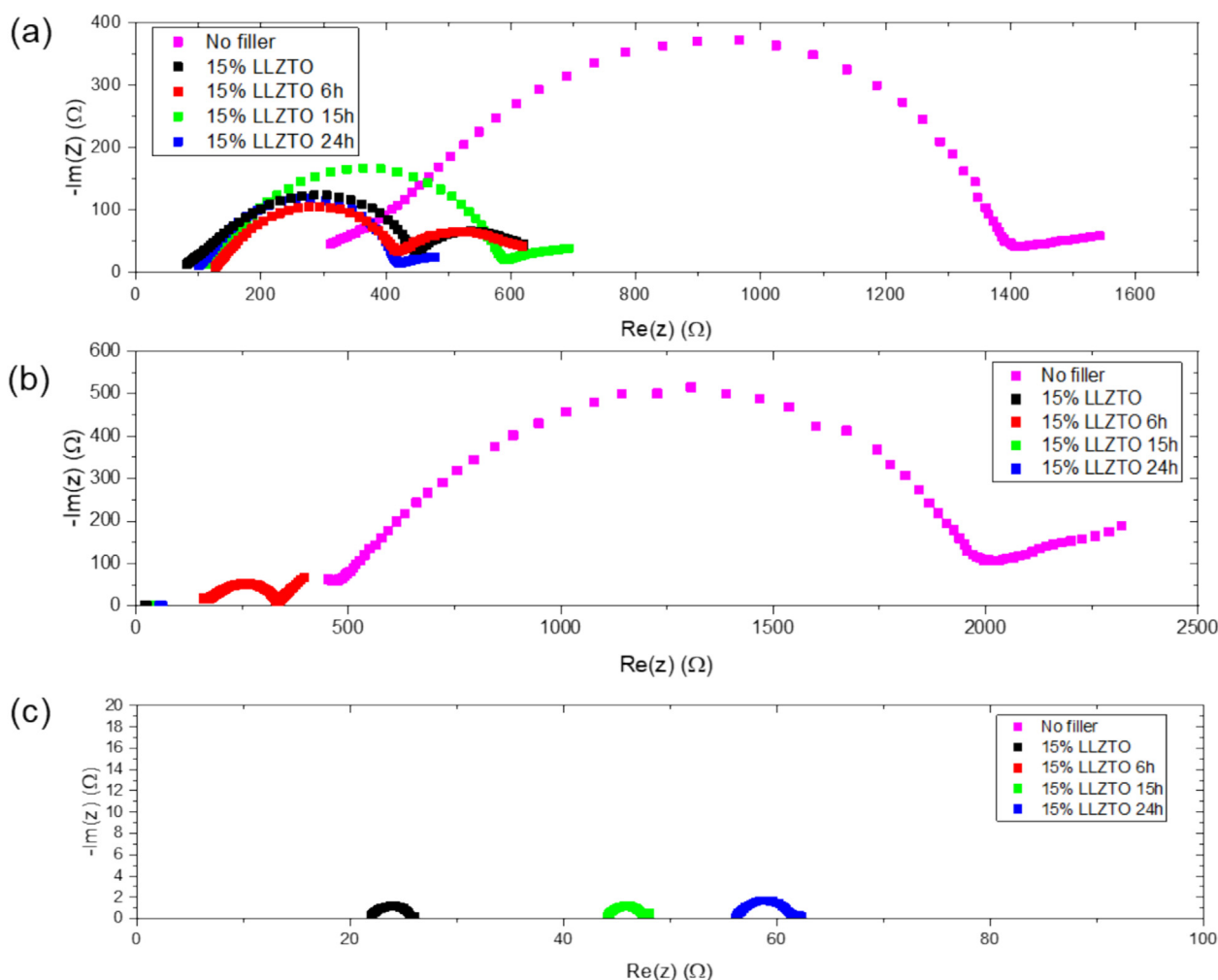

Fig. 7. Nyquist plots of EIS measurements on Li|IG|Li cells (a) before and (b) after the stripping/plating experiment shown in Fig. 6; (c) magnification of the high-frequency region depicted in (b).

membrane between a lithium-metal electrode and a stainless-steel blocking electrode. Fig. 5b shows the stability towards lithium metal calculated at 5 μA cm^{-2}. The insertion of the inorganic filler increased the oxidation potential from 4.65 to 4.98 V for 15% LLZTO 15 h and 24 h, while 15% LLZTO 6 h was stable up to 5.27 V. The extended ESW given by LLZTO 6 h is probably due to a better dispersion of functionalized inorganic particles within the IG, increasing the oxidation stability of the electrolyte, and has been

confirmed by a previous work on garnet particles functionalization [38].

To study the reversibility of the redox reaction occurring within the cell, IGs were characterized by means of cyclic voltammetry (CV) in the 2.5–4.2 V potential range. The results are presented in Fig. S7a–e, showing the typical CV plots for LFP with a delithiation peak at 3.65 V upon oxidation and a lithiation peak at 3.17 V upon reduction. The current intensity increased upon cycling, indi-
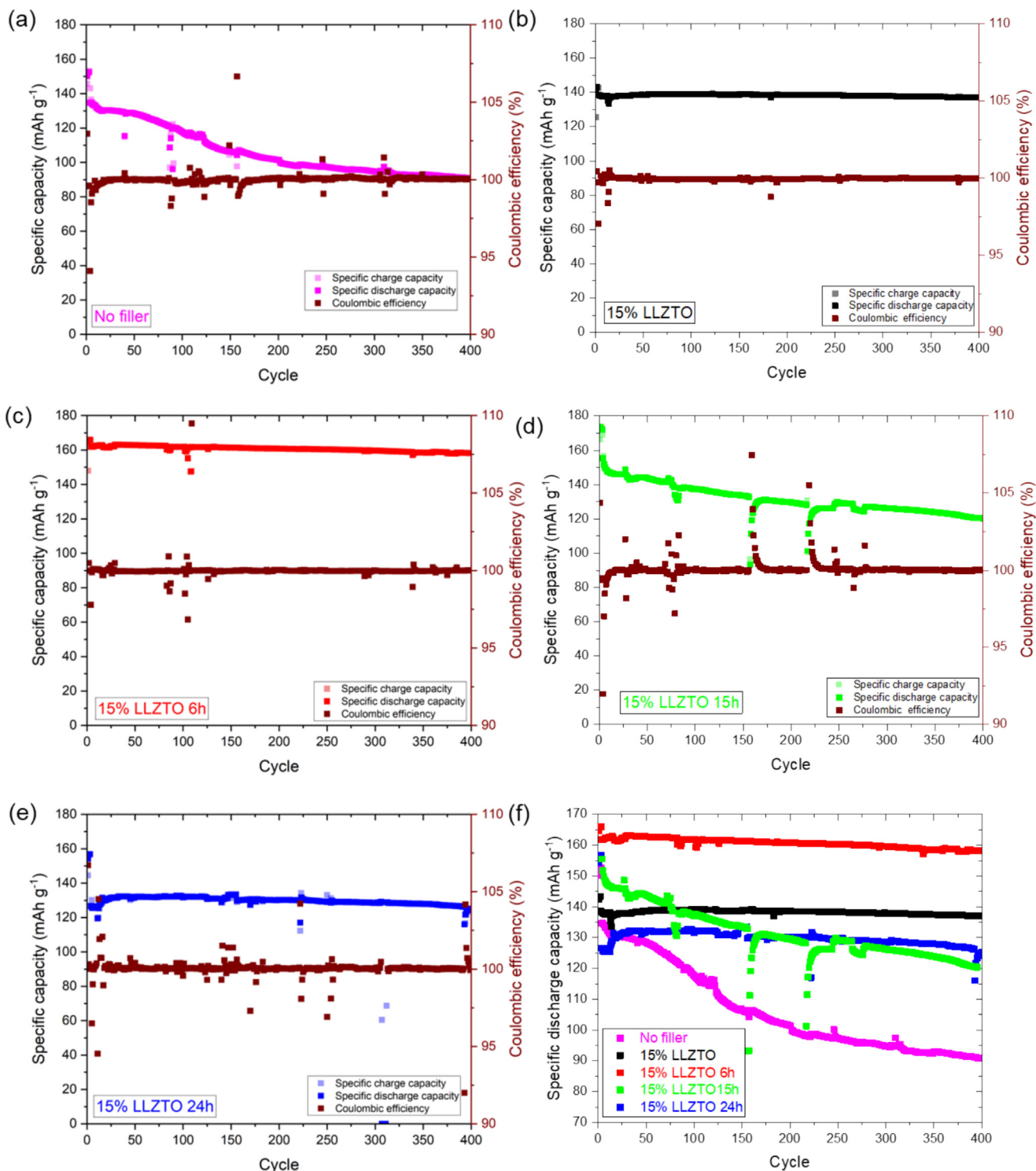
Fig. 8. Cycling performance in Li|IG|LFP cells, 3 cycles at 0.1C then 0.2C at 40°C with (a) 'no filler', (b) 15% LLZTO, (c) 15% LLZTO 6 h, (d) 15% LLZTO 15 h, and (e) 15% LLZTO 24 h. (f) Comparison of the specific discharge capacities upon cycling.

cating the presence of an activation process such as cathode wetting and/or electrolyte|electrode interface formation. Bare LLZTO and LLZTO 6 h reached reversible cycling after three cyclic sweeps, while in the other cases, the activation process took longer time. 15% LLZTO 6 h showed the highest specific current and area subtended by the curve, promising an improved cycling performance compared to the other formulations. 'No filler' and 15% LLZTO 24 h showed smaller lithiation/delithiation peaks and reversible cycling was reached after the 7th cycle, suggesting the formation of a non-optimum contact with the electrodes. The same behaviour was apparent from the lithium stripping/plating tests, for which symmetric Li|IG|Li cells were subjected to a constant current density for 1 h. As shown in Fig. 6a–d, 'no filler' and 15% LLZTO 24 h show a rising overpotential at 0.05 mA cm^{-2}, presumably due to an increase of the interfacial charge transfer resistance upon cycling. 15% LLZTO and 15% LLZTO 6 h show a rather stable overpotential of 40 mV almost half the one displayed by 'no filler', while in the case of 15% LLZTO 15 h a slightly higher and stable overpotential was observed. Subsequently, after 50 cycles the current was increased to 0.1 mA cm^{-2} and 15% LLZTO 6 h displayed a stable overpotential of 100 mV for 600 h.

In contrast, noisy voltage profiles were observed for all the other formulations, indicating a sluggish Li$^+$ transport in the electrolyte causing uneven lithium metal plating with the formation of a mossy surface. The voltage drops may suggest the growth of lithium dendrites and the formation of soft short circuits, as reported by Menkin et al. [47]. The reduced overpotential observed for 15% LLZTO at higher current density is likely due to the increased surface area caused by the uneven lithium deposition. Consequently, the local real surface area is much greater than the one measured before starting the test, leading to a decrease in overpotential. This behaviour suggests this formulation is not able to withstand a homogenous and even stripping/plating of lithium on the electrodes and this evolution often anticipates the short circuit of the cell. On the contrary, the formation of a stable interphase with lithium in the case of 15% LLZTO 6 h certainly plays a role for the observed better stripping/plating performances. An important impact factor for this is presumably the uniform distribution of the garnet particles and the improvement of filler/polymer interface. To confirm these hypotheses, EIS was conducted to monitor the IG|Li interphase before and after the stripping/plating test (Fig. 7). By comparing the impedance spectra it was possible to follow the evolution of the bulk resistance (R_b) and the charge-transfer resistance (R_{ct}) over time. Fig. S10 summarises the resistance values obtained by fitting EIS with ZView software. Generally, the composite IGs have a rather similar R_b, being slightly lower compared to 'no filler', thus, corroborating the beneficial effect of introducing LLZTO for achieving faster lithium transport within the electrolyte. The comparison of R_{ct} before cycling shows a greater difference between the studied IGs: 15% LLZTO 6 h shows one of the lowest value, indicating the formation of a beneficial electrode|electrolyte interface.

Conversely, the R_{ct} of 'no filler' is particularly high due to the formation of a non-optimal interface with the electrodes. After cycling, the EIS data display a significant reduction of R_b and R_{ct} for 15% LLZTO, 15 h and 24 h. This may be ascribed to the deposition of mossy lithium, leading to an increased electrode surface area, and eventually the formation of a soft short circuit. In this case, the coexistence of direct electron transport and interfacial reaction can deliver a misleadingly low overpotential [47], as shown in the stripping/plating voltage profiles. Meanwhile, 15% LLZTO 6 h shows a slight increase of R_b and a decrease of R_{ct} due to the possible decline of lithium conduction capabilities over cycling coupled with an improved electrolyte|electrode interface, while an increase of the electrode surface area cannot be excluded. The opposite trend is visible for 'no filler', for which the EIS data display an increase of R_b and R_{ct}, which can be justified by a worsening of the electrolyte bulk and interface.

The IGs' performance as electrolytes in LMBs was tested in Li|IG|LFP cells in the 2.5–4.2 V voltage range. The results are shown in Fig. 8a–f. Following an initial activation at 0.1C, the cells underwent cycling at 0.2C to monitor the long-term cycling stability. The cells assembled with bare LLZTO exhibit a stable cycling with an average Coulombic efficiency of 99.91% and a capacity retention of 99.9% after 200 cycles. 'No filler' showed a fast capacity decay, delivering a specific discharge capacity of 118 mA h g^{-1} after 100 cycles with a capacity retention of 72.2% after 200 cycles. In this case, the formation of a non-optimum interface has been shown in previous tests, as well as scarce lithium conduction capabilities. Conversely, 15% LLZTO 15 h displayed a large capacity retention of 83.3% after 200 cycles, while 15% LLZTO 24 h showed a rather stable cycling with a lower capacity delivered. The cells assembled with 15% LLZTO 6 h delivered a specific capacity of 162 mA h g^{-1} after 100 cycles with a capacity retention of 99.3% after 200 cycles. This IG showed very stable cycling and an average Coulombic efficiency of 99.93%. These results are in line with previous tests that highlight the fast Li$^+$ kinetics of this electrolyte coupled with the formation of a favorable interface with the electrodes. Such findings highlight the importance of TPM functionalization to remove the resistive Li$_2$CO$_3$ surface layer present on bare LLZTO NPs and to form an organic link to the polymeric backbone. Presumably, the thickness of the organic layer plays also a role in favouring fast Li$^+$ kinetics through the electrolyte, and in this case LLZTO 6 h provides an optimum in terms of ionic conductivity and cycling performance. Hence, the functionalization time of 6 h seems to be the optimum to reduce lithium leaching, while obtaining a viable functionalization layer.

4. Conclusions

Composite ionogels (IGs) were synthesized via a facile one-pot preparation protocol by mixing the monomers with an ionic liquid and LLZTO, yielding self-standing and flexible electrolyte membranes. A different degree of functionalization was applied to the LLZTO by grafting with TPM (3-(trimethoxysilyl) propylmethacrylate) and simultaneously removing the resistive Li$_2$CO$_3$/LiOH surface layer. An optimum filler distribution was obtained for 15% LLZTO 6 h, leading to a superior ionic conductivity of, e.g., >0.4 mS cm^{-1} at 20 °C and > 1 mS cm^{-1} at 40 °C, and high stability towards oxidation up to 5.3 V vs. Li$^+$/Li. Highly stable cycling was obtained for symmetric Li|IG|Li cells, showing a stable overpotential for 600 h at 0.1 mA cm^{-2}, and for Li|IG|LFP cells delivering > 160 mA h g^{-1} at 0.2C. These results underline the importance of tuning the interfacial layer between the polymer and the inorganic phase for the successful development of hybrid electrolyte systems for safer lithium-metal batteries.

CRediT authorship contribution statement

Matteo Gandolfo: Writing – review & editing, Writing – original draft, Methodology, Investigation, Formal analysis, Data curation, Conceptualization. **Mattia Longo:** Writing – review & editing, Investigation, Formal analysis, Data curation. **Thomas Diemant:** Writing – review & editing, Investigation, Formal analysis, Data curation. **Silvia Bodoardo:** Resources, Funding acquisition. **Dominic Bresser:** Writing – review & editing, Validation, Supervision, Resources, Methodology, Data curation, Conceptualization. **Julia Amici:** Writing – review & editing, Validation, Supervision, Resources, Project administration, Methodology, Investigation, Funding acquisition, Formal analysis, Data curation, Conceptualization.

Declaration of competing interest

The authors declare that they have no known competing financial interests or personal relationships that could have appeared to influence the work reported in this paper.

Acknowledgements

Appendix A. Supplementary material

Supplementary data to this article can be found online at https://doi.org/10.1016/j.jechem.2025.03.056.

References

[1] W. Li, B. Song, A. Manthiram, Chem. Soc. Rev. 46 (2017) 3006–3059.
[2] J. Xu, X. Cai, S. Cai, Y. Shao, C. Hu, S. Lu, S. Ding, EEM 6 (2023) e12450.
[3] J. Lu, T. Wu, K. Amine, Nat Energy 2 (2017) 1–13.
[4] X. Zhang, Y. Yang, Z. Zhou, Chem. Soc. Rev. 49 (2020) 3040–3071.
[5] S.K. Sharma, G. Sharma, A. Gaur, A. Arya, F.S. Mirsafi, R. Abolhassani, H.-G. Rubahn, J.-S. Yu, Y.K. Mishra, Energy Adv. 1 (2022) 457–510.
[6] J. Xiao, Q. Li, Y. Bi, M. Cai, B. Dunn, T. Glossmann, J. Liu, T. Osaka, R. Sugiura, B. Wu, J. Yang, J.-G. Zhang, M.S. Whittingham, Nat. Energy 5 (2020) 561–568.
[7] A. Varzi, K. Thanner, R. Scipioni, D. Di Lecce, J. Hassoun, S. Dörfler, H. Altheus, S. Kaskel, C. Prehal, S.A. Freunberger, J. Power Sources 480 (2020) 228803.
[8] D. Lin, Y. Liu, Y. Cui, Nature Nanotech 12 (2017) 194–206.
[9] R. Bhattacharyya, B. Key, H. Chen, A.S. Best, A.F. Hollenkamp, C.P. Grey, Nature Mater 9 (2010) 504–510.
[10] C. Monroe, J. Newman, J. Electrochem. Soc. 150 (2003) A1377.
[11] W. Zhao, J. Yi, P. He, H. Zhou, Electrochem. Energ. Rev. 2 (2019) 574–605.
[12] N. Wu, Y.-R. Shi, S.-Y. Lang, J.-M. Zhou, J.-Y. Liang, W. Wang, S.-J. Tan, Y.-X. Yin, R. Wen, Y.-G. Guo, Angew. Chem. Int. Ed. 58 (2019) 18146–18149.
[13] D.E. Fenton, J.M. Parker, P.V. Wright, Polymer 14 (1973) 589.
[14] M. Armand, M. Duclot, J. Chabagno, in: Proceedings of the Second International Meeting on Solid Electrolytes, St. Andrews, Scotland, 1978.
[15] Z. Hei, S. Wu, H. Zheng, H. Liu, H. Duan, Solid State Ion. 375 (2022) 115837.
[16] D. Bresser, S. Lyonnard, C. Iojoiu, L. Picard, S. Passerini, Mol. Syst. Des. Eng. 4 (2019) 779–792.
[17] Z. Luo, W. Li, J. Yan, J. Sun, Adv. Funct. Mater. 32 (2022) 2203988.
[18] M. Watanabe, M.L. Thomas, S. Zhang, K. Ueno, T. Yasuda, K. Dokko, Chem. Rev. 117 (2017) 7190–7239.
[19] K. Liu, Z. Wang, L. Shi, S. Jungsuttiwong, S. Yuan, Journal of Energy Chemistry 59 (2021) 320–333.
[20] M. Gouverneur, F. Schmidt, M. Schönhoff, Phys. Chem. Chem. Phys. 20 (2018) 7470–7478.
[21] F. Wu, N. Chen, R. Chen, L. Wang, L. Li, Nano Energy 31 (2017) 9–18.
[22] X. Li, Z. Zhang, L. Yang, K. Tachibana, S. Hirano, J. Power Sources 293 (2015) 831–834.
[23] J. Li, M. Jing, R. Li, L. Li, Z. Huang, H. Yang, M. Liu, S. Hussain, J. Xiang, X. Shen, ACS Appl. Polym. Mater. 4 (2022) 7144–7151.
[24] R. Chen, W. Qu, J. Qian, N. Chen, Y. Dai, C. Guo, Y. Huang, L. Li, F. Wu, J. Mater. Chem. A 5 (2017) 24677–24685.
[25] Y. Dai, S. Greenbaum, D. Golodnitsky, G. Ardel, E. Strauss, E. Peled, Y. Rosenberg, Solid State Ion. 106 (1998) 25–32.
[26] M. Gandolfo, D. Versaci, C. Francia, S. Bodoardo, J. Amici, Electrochim. Acta 463 (2023) 142857.
[27] J.B. Goodenough, H.-Y.-P. Hong, J.A. Kafalas, Mater. Res. Bull. 11 (1976) 203–220.
[28] X. Yu, A. Manthiram, Energy Storage Mater. 34 (2021) 282–300.
[29] Y. Ren, K. Chen, R. Chen, T. Liu, Y. Zhang, C.-W. Nan, J. Am. Ceram. Soc. 98 (2015) 3603–3623.
[30] C. Wang, K. Fu, S.P. Kammampata, D.W. McOwen, A.J. Samson, L. Zhang, G.T. Hitz, A.M. Nolan, E.D. Wachsman, Y. Mo, V. Thangadurai, L. Hu, Chem. Rev. 120 (2020) 4257–4300.
[31] M. Hou, F. Liang, K. Chen, Y. Dai, D. Xue, Nanotechnology 31 (2020) 132003.
[32] Z. Wan, D. Lei, W. Yang, C. Liu, K. Shi, X. Hao, L. Shen, W. Lv, B. Li, Q.-H. Yang, F. Kang, Y.-B. He, Adv. Funct. Mater. 29 (2019) 1805301.
[33] H. Deng, F. He, T. Liu, M. Ye, F. Wan, X. Guo, Nanotechnology 35 (2024) 195402.
[34] T. Panneerselvam, R. Murugan, S. O V, M. M, S. Elsin Abraham, Energy Fuels 38 (2024) 682–693.
[35] J. Zheng, Y.-Y. Hu, ACS Appl. Mater. Interfaces 10 (2018) 4113–4120.
[36] Y. Zhai, G. Yang, Z. Zeng, S. Song, S. Li, N. Hu, W. Tang, Z. Wen, L. Lu, J. Molenda, ACS Appl. Energy Mater. 4 (2021) 7973–7982.
[37] Q. Guo, Y. Han, H. Wang, S. Xiong, Y. Li, S. Liu, K. Xie, ACS Appl. Mater. Interfaces 9 (2017) (1844) 41837–141834.
[38] C. Yan, P. Zhu, H. Jia, Z. Du, J. Zhu, R. Orenstein, H. Cheng, N. Wu, M. Dirican, X. Zhang, Energy Storage Mater. 26 (2020) 448–456.
[39] L. Zhang, H. Guo, Q. Zhang, A. Wang, Y. Su, Y. Chen, Y. Li, F. Shen, X. Han, Energy Fuels 37 (2023) 14341–14349.
[40] A. Sharafi, S. Yu, M. Naguib, M. Lee, C. Ma, H.M. Meyer, J. Nanda, M. Chi, D.J. Siegel, J. Sakamoto, J. Mater. Chem. A 5 (2017) 13475–13487.
[41] H. Kim, H.D. Jang, M. Choi, Chem. Eng. J. 280 (2015) 132–137.
[42] L. Chen, Y. Li, S.-P. Li, L.-Z. Fan, C.-W. Nan, J.B. Goodenough, Nano Energy 46 (2018) 176–184.
[43] H. Gan, J. Sun, Y. Xia, P. Qiu, L. Li, W. Zhu, J. Phys. Chem. C 127 (2023) 21015–21021.
[44] J. Zhang, N. Zhao, M. Zhang, Y. Li, P.K. Chu, X. Guo, Z. Di, X. Wang, H. Li, Nano Energy 28 (2016) 447–454.
[45] H. Zhuang, W. Ma, J. Xie, X. Liu, B. Li, Y. Jiang, S. Huang, Z. Chen, B. Zhao, J. Alloy. Compd. 860 (2021) 157915.
[46] J. Vila, P. Ginés, J.M. Pico, C. Franjo, E. Jiménez, L.M. Varela, O. Cabeza, Fluid Phase Equilib. 242 (2006) 141–146.
[47] S. Menkin, J.B. Fritzke, R. Larner, C. de Leeuw, Y. Choi, A.B. Gunnarsdóttir, C.P. Grey, Faraday Discuss. 248 (2024) 277–297.